Volume 1 | Number 1 | Jan 2013 | Pages 1–100

Dalton Transactions

An international journal of inorganic chemistry
www.rsc.org/dalton

ROYAL SOCIETY OF CHEMISTRY

ROYAL SOCIETY OF CHEMISTRY

www.rsc.org/dalton

Dalton Trans.

Dalton Transactions

Dynamic Article Links ▶

ARTICLE TYPE

Effects of crystalline phase and morphology on the visible light photocatalytic H₂-production activity of CdS nanocrystals

Di Lang, Quanjun Xiang*, Guohong Qiu, Xionghan Feng, and Fan Liu*

Visible light photocatalytic H₂-production from aqueous solutions is of great importance for its potential application in converting solar energy into chemical energy. In this study, a series of CdS nanostructures with different content of wurtzite (WZ) and zinc blende (ZB) phase were successfully synthesized by a simple solvothermal route in an ethylenediamine and ethylene glycol mixed solution. The solvent volume ratio of ethylenediamine in the mixed solution (*R*) exhibited an obvious influence on the crystalline phase and 10 morphology of the resulting CdS products. With increasing *R*, the percentage of wurtzite first increased and then decreased, whilst the morphology changed from nanoparticles to multi-armed nanorods, and finally to long rods and sheets. The prepared multi-armed CdS nanorods samples showed especially high and stable photocatalytic H₂-production activity with Pt (0.25 wt%) as co-catalyst and lactic acid aqueous solution as sacrificial reagent under visible light irradiation. The optimized CdS nanorods with the highest percentage (64%) of WZ phase exhibited a high H₂-production rate of 231.4 μmol h⁻¹ (about 16.6 times higher than that of CdS nanoparticles with low 15 percentage (38.4%) of WZ CdS) and with a quantum efficiency (QE) of 28% at 420 nm. This high photocatalytic H₂-production activity could be attributed to the results of the positive synergistic effects of hexagonal WZ phase and morphology of multi-armed nanorods.

Introduction

20 Photocatalytic H₂-production from water splitting using semiconductor photocatalysts is of great interest due to its possible application for the conversion of solar energy into chemical energy.[1-6] Since Fujishima and Honda first reported the photocatalytic splitting of water on TiO₂ electrodes in 1972,[7] this 25 process attracted great attention in the development of highly active and stable semiconductor photocatalysts to produce clean and renewable hydrogen by water splitting using solar energy.[8-10] However, most of the photocatalysts developed for splitting water can solely absorb UV-light that only takes up ca. 4% of the total 30 sunlight, resulting in low light utilization efficiency, which severely restricts its practical applications.[11] Therefore, it is highly desirable to develop visible-light-driven photocatalysts for hydrogen production under sunlight irradiation. Chalcogenides are regarded as good candidates for photochemical water splitting 35 because of their catalytic function and suitable bandgap. Particularly, CdS is probably one of the most studied metal sulfide materials as a photocatalytic H₂-production catalyst. Because CdS has a relatively narrow bandgap (2.4 eV), which can efficiently absorb visible light, and its band edge is more 40 negative than the reduction potential of protons.[12,13] For example, Bao et al. reported that the nanoporous CdS nanostructures loaded with monodisperse 3-5 nm Pt nanocrystals reached the highest photocatalytic activity which had a high apparent quantum efficiency of about 60.34% at 420 nm.[14] Li et al. found 45 the CdS cluster coupled with graphene sheets as photocatalysts loading 0.5 wt % Pt as a cocatalyst for increased photocatalytic

H₂-production with an apparent quantum efficiency of about 22.5% at 420 nm.[15]

In recent years, CdS nanostructures have been of academic 50 interest and particular industrial due to their distinctive morphologies, peculiar and fascinating physicochemical properties.[16] Particularly, it has been proved that the photocatalytic activity of CdS nanomaterials is strongly dependent on its crystalline phase, morphology, specific surface 55 areas, pore structure, and crystallite size.[17-19] To date, although CdS with different phase structures and varying morphologies have been synthesized and investigated in previous studies, the effects of crystalline phase and morphology of CdS on photocatalytic activity has received only sporadic. For instance, 60 Bao et al. reported the effects of phase structure and composition of the CdS nanocrystals on the photocatalytic H₂-production efficiency.[20] Muruganandham et al. reported the synthesis of microtowers and octahedral geometric CdS nanostructures and their photocatalytic H₂-production activity.[21] However, effects of 65 crystalline phase and morphology on the photocatalytic H₂-production activity of CdS nanocrystals were seldom reported in these previous studies. Therefore, it is necessary to make a thorough inquiry of the effects of the morphology and crystalline phase on the photocatalytic activity of CdS.

70 In fact, the crystalline phase determines the crystal structure, electronic structure and surface atomic geometry, and thus impact on the photoinduced redox processes.[16,22] For example, the well-known material, Degussa P25 TiO₂, which consist of 80% anatase and 20% rutile，has the high photoreactivity due to the 75 combined effects of anatase and rutile mixed phases.[23,24] Compared with the TiO₂, CdS has two common crystalline phases of a stable wurtzite (WZ-hexagonal phase) and a

metastable zinc blende (ZB-cubic phase).[25,26] In particular, the WZ and ZB CdS have different optical and electronic properties. Therefore，it is very useful to find an appropriate content of WZ in order to obtain a preferable performance in photocatalytic H_2-evolution property of CdS. Due to the fact that the morphology is accompanied by the crystal growth, the effect of morphology and phase should be discussed together. In the present work, we report the synthesis of CdS nanostructures with different content of WZ and ZB phase through a simple solvothermal route and their photocatalytic hydrogen production activity from lactic acid aqueous solution with Pt as a co-catalyst under visible-light irradiation. This work highlights the synergetic effect of crystalline phase and morphology of CdS in improving visible light photocatalytic H_2-production activity of CdS nanomaterials. Some relevant factors, such as specific surface area, size and crystallinity on the photocatalytic H_2-production properties of the CdS nanostructures were discussed and investigated. Above all, the combined effects of crystalline phase and morphology on photocatalytic H_2-production activity have been discussed. From what we understand, this is the first time to report the influence of crystalline phase and morphology on the visible-light photocatalytic H_2-production activity of CdS nanocrystals. This work may provide new insights for the preparation of highly photocatalytic activity CdS nanomaterials.

Experimental section

Sample preparation

All reagents were of analytical grade and used without further retreatment. Ultrapure water was used in the whole experiments. In a typical synthesis of CdS nanomaterials, cadmium acetate ($Cd(CH_3COO)_2 \cdot 2H_2O$, 1.4 mmol) was dissolved in 60 mL aforehand mixed solvents of ethylenediamine (en) and ethylene glycol (EG) under magnetic stirring to form a clear solution. After that, thioacetamide (CH_3CSNH_2, 2.0 mmol) was added into the above mixed solution. After stirring for 1 h, the mixed solution was then transferred into a dried 100 mL Teflon-lined autoclave and maintained at 180 °C for 5 h. Next, the autoclaves were cool to room temperature naturally, and the yellow precipitates were collected by centrifugation and rinsed several times with ultrapure water and absolute alcohol alternately. The final product was dried at 60 °C for 10 h. The volume ratios of en to the mixed solution (en + EG), which hereafter was designated as ***R***, were 0, 5, 15, 25, 50, 75 and 100 % (vol %) (see Table 1), and the resulting samples were labeled as R0, R5, R15, R25, R50, R75 and R100, respectively. To investigate the effect of the CdS phase on photocatalytic performance, CdS-WZ sample was prepared by hydrothermal method in ethylenediamine solution with $Cd(NO_3)2 \cdot 4H_2O$ and NH_2CSNH_2 as precursors.[27] The autoclave was maintained at 160℃ for 48 h to obtain the pure WZ phase of CdS. In order to study the effect of morphology, the above-prepared CdS-WZ and R50 samples were manually milled by agate mortar, and the obtained samples were denoted as CdS-WZ/M and R50/M, respectively. To obtain the pure WZ R50 sample, the resulting R50 powder was placed in a tube furnace and heated in a flow of N_2 at 350℃ for 2 h, which was labeled as R50-WZ.[28]

Characterization

The crystalline phases of the obtained samples were determined by powder XRD measurements performed on a Bruker D8 Advance diffractometer. Each sample powder was scanned through a 2 θ range of 10-70° using Ni-filtered Cu Kα radiation (k = 0.15418 nm) with an operation voltage and current maintained at 40 kV and 40 mA, respectively .The scanning rate is 8° min⁻¹ at a step size of 0.02. Transmission electron microscopy (TEM) images were obtained by using Hitachi-7650 (HITACHI, Japan) transmission electron microscopes operated at 120 kV. The high-resolution transmission electron microscopy (HRTEM) analyses were conducted with a JEM-2100F (JEOL, Japan) electron microscope, using a 200 kV accelerating voltage. The UV-vis diffused reflectance spectra were obtained for the dry-pressed disk samples using a UV-vis spectrophotometer (Shimadzu 2450 PC) equipped with an integrating sphere accessory (ISR1200). $BaSO_4$ was used as a reflectance standard in a UV-vis diffuse reflectance experiment. The specific surface area (SSA) of the powders was evaluated from N_2 adsorption and desorption isotherms measured on an Autosorb-1 standard physical adsorption analyzer (Quantachrome Autosorb-1). The samples were degassed at 110 ℃ for 3 h under vacuum prior to adsorption measurement. The SSA was calculated by the Brunauer-Emmett-Teller (BET) method using adsorption data in the relative pressure (P/P_0) range of 0.05–0.3. The desorption isotherms was used to determine the pore size distribution via the Barrett–Joyner–Halenda (BJH) method.[29]

Photocatalytic H_2-production activity

The photocatalytic H_2-production experiments were conducted in a 100 mL gas-closed Pyrex flask (the three openings of the flask were sealed with silicone rubber septum) with outer irradiation at ambient temperature and atmospheric pressure. A 350 W Xe arc lamp which equipped with an UV-cutoff filter ($\leqq 420$ nm) was used as a visible-light source (15 cm far away from the photocatalytic reactor). The focused intensity on the flask was ca. 70 mW cm⁻², which was measured by a visible-light radiometer (Model: FZ-A, China) in the wavelength range of 420-1000 nm. Before the reaction, a definite concentration of $H_2PtCl_6 \cdot 6H_2O$ aqueous solution was dripped into the system to load 0.25 wt % Pt onto the surface of the photocatalyst by a photodeposition method. A 50 mg portion of the photocatalyst was suspended in 80 mL of an aqueous solution containing 10 mL lactic acid under magnetic stirring. Before irradiation, the system was bubbled with N_2 for 0.5 h to remove the dissolved oxygen. Continuous magnetic stirrer was applied at the bottom of the reactor in order to keep the photocatalyst particles in suspension status during the whole experiment. A 0.4 mL of gas was sampled intermittently through the septum after 60 min side-irradiation, and the amount of hydrogen was analyzed by gas chromatograph (GC-14C, TCD, N_2 carrier, molecular sieve 5Å, Shimadzu, Japan). The apparent quantum efficiency (QE) was measured under the same photocatalytic reaction conditions except that the light source was different. Two low power UV-LEDs (3 W, 420 nm, Shenzhen Lamplic Science Co. Ltd., China), which were positioned 1 cm away from the reactor in two sides, were used as light sources to trigger the photocatalytic reaction. The areas and focused

intensity on the flask for each UV-LED was 1 cm^2 and ca. 6.0 mW cm^{-2}, respectively. The QE was calculated using the following equation:

$$QE[\%] = \frac{\text{number of reacted electrons}}{\text{number of incident photons}} \times 100 \qquad (1)$$

$$= \frac{\text{number of evolved H}_2 \text{ molecules} \times 2}{\text{number of incident photons}} \times 100$$

[5] **Photoelectrochemical measurements**

Photocurrent was measured on an electrochemical analyzer (CHI660E, Shanghai Chenhua limited, China) in a standard three-electrode system using Ag/AgCl (saturated KCl) as a reference electrode, Pt wire as the counter electrode, the prepared samples [10] as the working electrodes, and 0.5 M Na$_2$SO$_4$ as electrolyte. A 350 W Xe arc lamp through a cutoff filter ($\leqq$ 420 nm) served as a light source and the integrated light intensity was 70 mW cm^{-2}. The working electrodes were prepared as follows: 0.05 g polyethylene glycol (PEG, molecular weight: 20000) was grinded [15] with 0.05 g of photocatalyst and 0.5 mL ethanol to make a slurry. The slurry was then coated onto a 2 cm×1.2 cm F-doped SnO$_2$-coated glass (FTO glass) electrode by the doctor blade method. Then, the resulting electrodes were dried in an oven at 100 ^{o}C for 30 min.

[20] **Results and discussion**

Crystalline phase and morphology

The crystalline phase and crystallinity of CdS nanomaterials are of significant importance for its photocatalytic H$_2$-production activity. XRD was used to investigate the changes of crystalline [25] phase and crystallization of the prepared CdS samples with different **R** in mixed solvent. Figure 1a displays the influence of **R** on crystalline phase of the obtained CdS samples in the en and EG mixed solution with varying **R**. As seen from this figure, all the diffraction peaks can be easily indexed to the hexagonal WZ [30] (JCPDS No. 01-089-2944) and cubic ZB (JCPDS No. 01-089-0440) of CdS, and no diffraction peaks of impurities are found, implying that the obtained products are pure CdS with a mixture of cubic and hexagonal phases. Further observation displays that with the increase of **R**, the intensity of (002) diffraction peak [35] increases and there is a simultaneous reduction of width, indicating the enhancement of crystallization. The strong and narrow (002) diffraction peak also indicates that the CdS nanocrystals have a preferential orientation growth in the [001] direction (along the *c*-axis). Notably, it also can be seen that with [40] increasing **R**, the relative ratio of the characteristic (101) peak (2θ = 28.33°) of WZ to the diffraction peaks (2θ = 26.51°) of both WZ and ZB increased. This strongly indicated that with increasing **R**, the hexagonal WZ phase increases while the cubic ZB phase decreases in the products.

[45] Figure 1b shows the XRD patterns of the sample prepared at **R** < 25%. The peaks corresponding to WZ CdS is dominant for samples prepared at R < 25%, but there is a small amount of the characteristic peak of ZB phase found in the sample prepared in pure EG solvent condition (**R** = 0). The minor peak at 2θ = 30.75° [50] corresponds to the (200) plane diffraction of the ZB phase of CdS (JCPDS No. 01-089-0440). The characteristic diffraction peak of
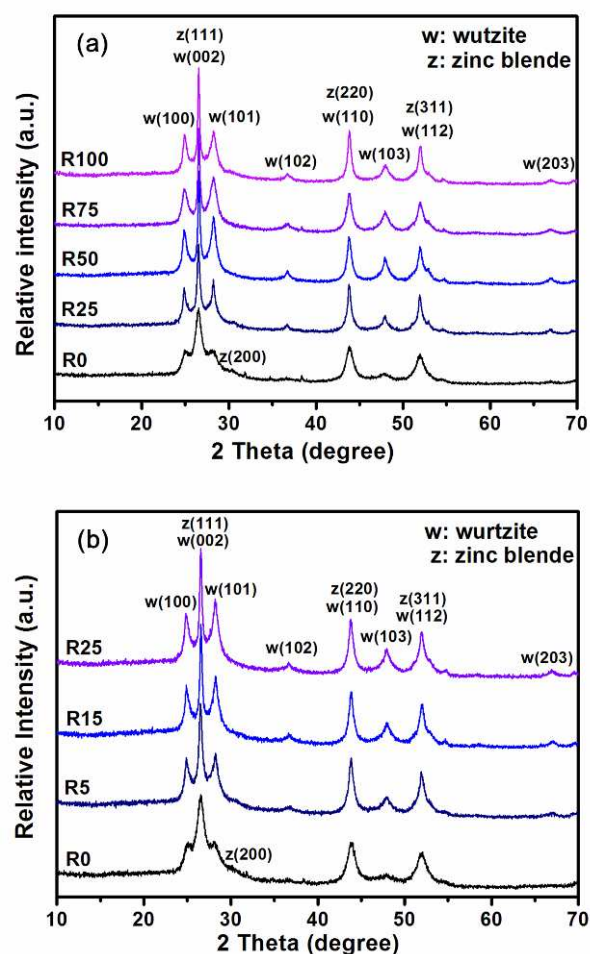

Figure 1. XRD patterns of (a) the R0, R25, R50, R75, R100 samples and [55] (b) the samples prepared at low R value (R = 0, 5, 15 and 25%).

the ZB phase disappears in the presence of en. It can be concluded that en is beneficial for the formation of WZ CdS and EG is in favor of the formation of ZB CdS.[30] Since no obvious peaks of ZB phase could be found in XRD patterns for the all [60] CdS samples studied, the phase content of the CdS sample can be approximately calculated from the integrated intensities of (110) and (103) planes of the WZ phase.[31] The intensity of (110) peak at 2θ = 43.9° is contributed by both ZB and WZ phases of CdS, while the intensity of the (103) peak at 2θ = 48.1° is only [65] assigned to the WZ phase CdS. Herein, the ratio of the intensity of the (103) and (110) peaks from standard XRD patterns of WZ CdS (JCPDS No. 01-089-2944) is 0.96. This suggest that WZ phase CdS has almost the same contribution to both peaks at 2θ = 48.1° and 2θ = 43.9°. Therefore, the content of WZ can be [70] calculated using the relative ratio of the intensity of the (103) and (110) peaks from semi-quantitative analysis by XRD EVA Software, which is similar with the calculation method in the literature.[31,32] Table 1 shows the calculated results. It can be seen that with increasing **R**, the hexagonal WZ phase increases while [75] the cubic ZB phase decreases in the products. Especially, the percentage of WZ phase in the products reached the highest value at **R** = 50%. With further increasing **R**, the percentage of hexagonal WZ phase decreased.
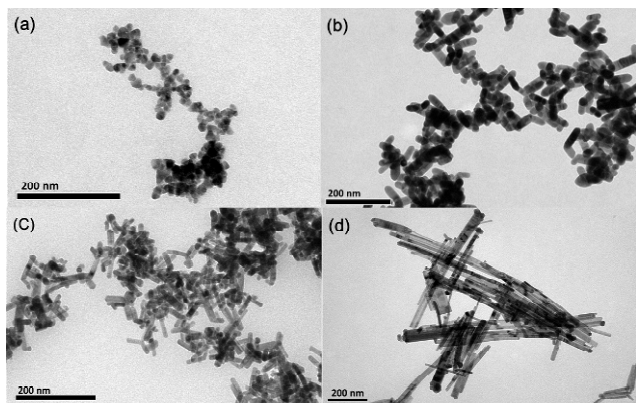
Figure 2. TEM images of the samples (a) R0, (b) R5, (c) R25 and (d) R100. Scale bar = 200 nm.

The microstructure of the CdS samples was further analyzed by TEM and HRTEM. Figure 2 shows TEM images of the CdS samples prepared at different *R* (sample R0, R5, R50 and R100). In the absence of en, the obtained product is nanoparticles in an agglomerated status (Figure 2a). At *R* = 5%, some nanorods with a average size of about 40 nm appears (see Figure 2b), implying that the presence of en had a significant influence on the particle morphology. Increasing *R* to 50% produces multi-armed nanorods (see Figure 2c). When the en concentration increases to *R* = 100%, the multi-armed nanorods almost disappear and some long rods and sheets are produced (Figure 2d).
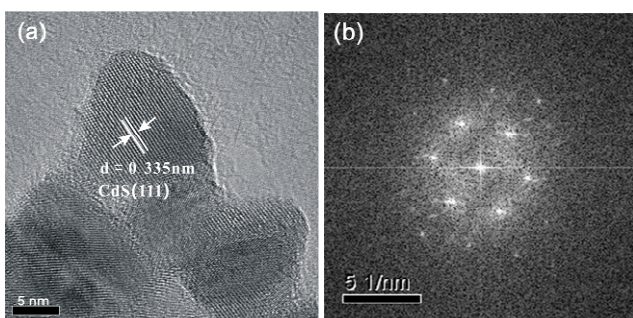
Figure 3. HRTEM (a) and FFT pattern (b) of the R0 sample. Scale bar = 5 nm.

Figure 3a displays the HRTEM image of the R0 sample. It shows clear lattice fringes and can make the identification of crystallographic spacing. The lattice fringes with a *d* spacing of ca. 0.335 nm can be assigned to the (111) lattice planes of cubic ZB CdS. The corresponding local fast-Fourier transformation (FFT) patterns (see Figure 3b) confirm that the non-order nanoparticles are single crystalline structure. TEM image (Figure 4a) shows that the R50 sample consists of well-defined multi-armed CdS nanorods with the lengths and diameters of ca. 35-50 and 8 nm, respectively. The corresponding HRTEM image (see Figure 4b) shows the lattice fringes which are vertical to one of the arms. The lattice spacing is *ca.* 0.335 nm, corresponding to the (002) lattice planes of hexagonal WZ CdS, which confirms that CdS nanorods grow along the *c*-axis [001] direction. Significantly, according to the lattice fringes of two {111} faces
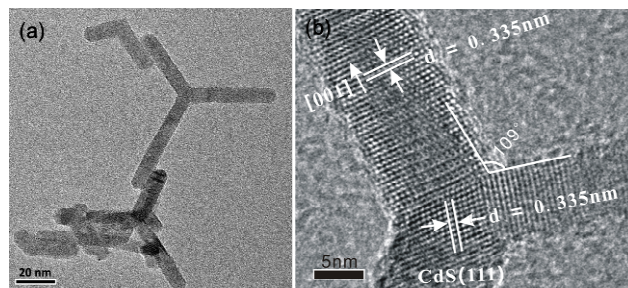

Figure 4. TEM (a) and HRTEM images (b) of the R50 sample.

and the tetrahedral geometry with a separation angle of ~109° between the arms of the tripods, it distinctly reveals that the core of multi-armed nanorods is of ZB CdS structure.[33,34] Therefore, the HRTEM image recorded on the nuclei and common boundary of multi-armed structures with good crystallinity and well-resolved lattice fringes demonstrates that the prepared CdS samples are not simple mixture of WZ and ZB CdS, but intergrowth crystal of two phase.

According to the above XRD and TEM results, it can be revealed that morphological evolution of the CdS nanostructure is strongly dependent on the en concentration in the reaction system. In the absence of en, the nucleation and growth of CdS particles is the equivalent crystal planes due to the similar growth rate of these planes. Therefore, the non-order nanoparticles are observed. When en concentration is low, en molecules can coordinate with Cd^{2+} and can slow the growth speed of some crystal planes, resulting in the form of a specific CdS shape. This is because that the different planes of CdS nanocrystals possess different adsorption ability of en. In our study, some short nanorods can be observed when the ratio of en was 5% (*R* = 5%). This implies that en can make the one-dimensional growth of CdS nanocrystals.[35] With further increasing the ratio of en (15-50%), more en molecules are adsorbed and gradually accumulated on the surfaces of CdS nanocrystals because of the strong coordination interaction between en and Cd^{2+}, and the CdS nanocrystals adopt a cubic ZB structure at the initial stage of nucleation, and then transform to the bulk stable WZ structure during growth process, resulting in the appearance of multi-armed nanostructures.[32] This growth mechanism of the multi-armed nanorods was correspond with the typical model in the literature.[36] Therefore, it is not surprising that the core of multi-armed nanorods is of ZB CdS structure. When the ratio of en increases over 50%, there are higher concentrations of en than that of Cd^{2+}. Under this Condition, The diffusion-limited aggregation (DLA) mechanism would be better to explain the crystal growing stage.[37] Combined with the aforementioned one-dimensional inducement by en, the intense exchange and diffusion among the growing rods will lead to the formation of long rods. So, it can be reasonable to deduce that the higher en concentration can promote the growth of crystals along [001] direction (along the *c*-axis).

UV-vis diffuse reflectance spectra

Figure 5 shows the UV-vis diffuse reflectance spectra of the CdS samples prepared at different *R* (sample R0, R5, R25, R50 and R100).For the R0 sample, a remarkable increase in the absorption intensity of wavelength shorter than 520 nm coincides with the
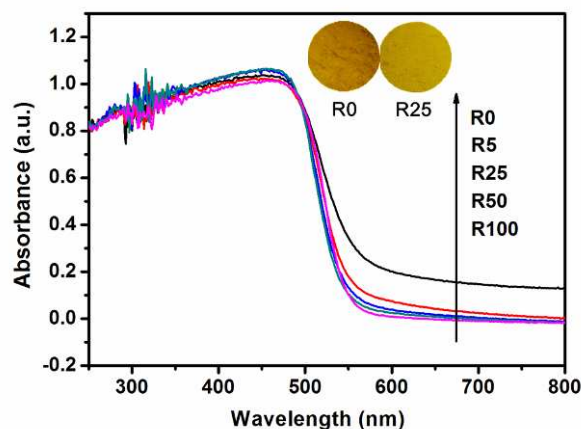
Figure 5. UV-vis diffuse reflection spectra of the R0, R5, R25, R50 and R100 samples. The insets show the colors of the R0 and R25 samples.

intrinsic bandgap of CdS ($\approx$ 2.4 eV). A comparison of absorption
5 spectrum of the R0 sample with those obtained for the aforementioned other four samples studied (sample R5, R25, R50 and R100) shows that the former exhibit a broad background absorption in the visible-light region (600-800 nm).The corresponding color of the R0 sample is darker than that of the
10 other four samples (inset in Figure 5). This can be ascribed to the difference of the crystalline phase in the R0 sample and the other four samples studied. A further observation implies that the four samples (sample R5, R25, R50 and R100) show an obvious blueshift of the absorption edge as that of the R0 sample,
15 indicating an increase in the bandgap energy of the CdS nanorods samples. The previous literature indicates that the bandgap of WZ CdS is higher than that of ZB CdS.[20,38] Therefore, this blueshift can be ascribe to the increasing proportion of WZ structure in the R5, R25, R50 and R100 samples, which coincides with the above
20 reported XRD results. According to the Kubelka-Munk method,[39,40] the bandgap for pure ZB CdS and for the mixture of ZB and WZ CdS (sample R0) is 2.36 and 2.41eV, respectively, which further support the previous study that the bandgap of WZ CdS is higher than that of ZB CdS.[41] This also implies that the
25 photogenerated holes and electrons on WZ CdS has larger oxidation and reduction powers than the photogenerated holes and electrons on ZB CdS for photocatalytic reactions, respectively.

Table 1. Summarized morphologies, percentage of crystalline phases,
30 sizes and specific surface area of the samples obtained under different solvent composition.

Samples	Ratio of en	Morphology	WZ phase (%)	Rod size (Length×Diameter) (nm)	SSA (m²/g)
R0	0%	Tetrahedron-like nanoparticles	38.4	16	108
R5	5%	Short rods	46.9	41×26	96
R15	15%	Multi-armed rods	49.5	34×13	97
R25	25%	Multi-armed rods	55.1	38×12	71
R50	50%	Multi-armed rods	64.0	161	78
R100	100%	Long rods and sheets	50.6	158	42

BET surface areas and pore size distribution

The BET specific surface areas and porous structures of the CdS samples prepared at different *R* were investigated by N_2
35 adsorption-desorption. Figure 6 displays N_2 adsorption-desorption isotherms and the corresponding pore-size distributions (inset) of the R0, R50 and R100 samples. The N_2 sorption isotherms of the aforementioned three samples could be assigned as type IV isotherms (according to IUPAC classification)
40 at relative pressure range of 0.5 to 0.8, implying the presence of mesopores (2 - 50 nm).[29] The shape of hysteresis loops of the R0 sample is of type H2, which belong to the ink-bottle-like pores with narrow necks and wider bodies.[29,42] While the isotherms of the R100 sample exhibit H3 hysteresis loops associated with
45 aggregates of one-dimensional nanostructure giving rise to slit-like pores. The pore size distributions curves (inset in Figure 6) of the aforementioned three samples exhibit a wide pore size distribution, further proofing the presence of mesopores. Especially, it is interesting to observe that the R50 sample
50 displays a bimodal pore-size distribution, which is consisted of fine intra-aggregated pores with a maximum pore diameter of 12 nm, and larger inter-aggregated pores with a maximum pore diameter of 19 nm. This also implies that the R50 sample with multi-armed nanorods are more beneficial for the formation of
55 porous structures than CdS nanopaticles and nanosheets, which will be useful in photocatalytic hydrogen production as they would provide efficient transport pathways to the interior void space.[43]

60
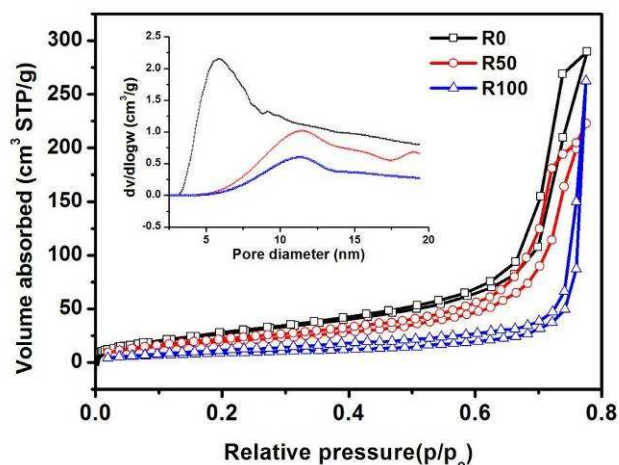
Figure 6. Nitrogen adsorption-desorption isotherms and the corresponding pore size distribution curves (inset) of the R0, R50 and R100 samples.

Photocatalytic activity

65 Photocatalytic H_2 production with the obtained CdS samples loaded with 0.25 wt. % Pt were recorded under visible-light irradiation (> 420 nm) using lactic acid as scavenger. Blank experiments showed no appreciable H_2 evolution in the absence of either photocatalyst or irradiation, implying that H_2 was
70 produced *via* photocatalytic reactions. The comparison of the visible-light photocatalytic H_2-production rates of the R0, R5, R15, R25, R50, R75 and R100 samples are shown in Figure 7a. For the CdS nanopaticles prepared in pure EG solution, the R0 sample displayed an obvious photoactivity and the H_2-production
75 rate reaches 13.9 μmol h^{-1}, owing to the suitable bandgap and catalytic function of CdS photocatalyst. In the presence of en, the

photocatalytic H_2-production activity of the prepared CdS samples was remarkably enhanced. At R = 50%, the H_2-production rate of the R50 sample achieves the highest value of 231.4 μmol h^{-1} with a 28% apparent quantum efficiency at 420
5 nm. In this respect, the H_2-production rate of the R50 sample is significantly greater than that of most semiconductor photocatalysts，exceeding that of R0 by a factor of 16.6. With further increasing the values of R, the photocatalytic activity decreases dramatically. In addition, the photocatalytic H_2-
10 production activity of the prepared CdS samples without using Pt as co-catalysts was also tested and compared, and the corresponding H_2-production rate was about one order of magnitude lower than the yields of the corresponding CdS samples with loading 0.25 wt % Pt. Generally speaking, metal
15 sulfides are not stable during the photocatalytic reaction and subjected to photocorrosion because S^{2-} is more susceptible to oxidation than water. In general, common hole scavengers such as methanol and ethanol are excellent fuels themselves and thus their utilization as hole scavengers is meaningless.[44,45] Thus,
20 lactic acid was selected in this work as the holes scavenger to suppress the photocorrosion of the CdS because it is a non-biodegradable pollutant and usually present in waste water
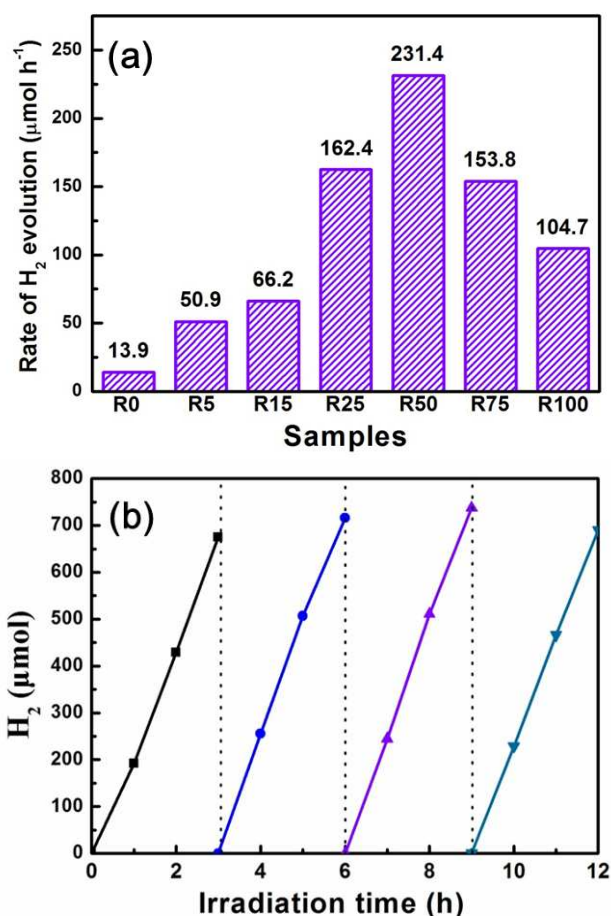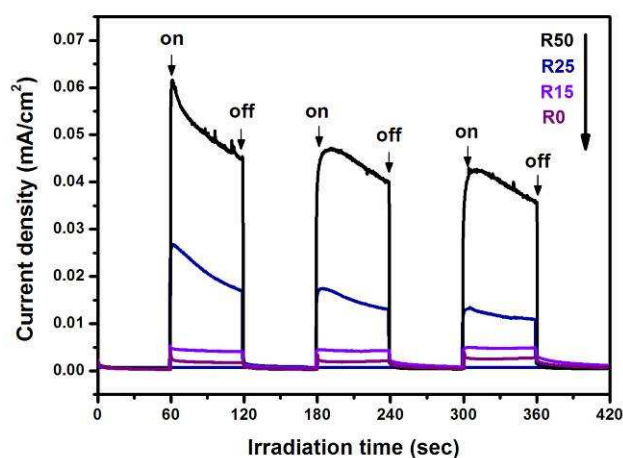

generated by oil production. The photostability of the multi-
30 armed CdS nanorods (sample R50) was investigated by performing recycling experiments of the photocatalyst (see Figure 7b). It is interesting to observe that the photocatalytic H_2-production rate of the R50 sample was enhanced after the first 3 h of the reaction. This is because the reaction of photocatalytic H_2-
35 production is an activated process, and the number of photons absorbed on the surface of photocatalysts increases with increasing irradiation time, which facilitates the photocatalytic production of H_2.[46] Furthermore, after four recycles, no obvious decrease in the photocatalytic H_2-production activity was
40 observed for R50, implying that it was not photo-corroded and was suitable for hydrogen generation from lactic acid aqueous solution.

Previous work has shown that many properties of CdS nanomaterials, such as morphology, crystalline phase,
45 crystallinity, specific surface area and defect, can affect its photocatalytic performance.[47] Among all the samples, the R50 sample shows the highest photocatalytic activity, which obviously exceeded the R0 sample. One possible explanation for this enhancement is the big difference in phase composition in the
50 R0 and R50 samples (see Table 1). The WZ CdS is very effective in promoting photocatalytic H_2-evolution from lactic acid water solution. This is because the photogenerated holes and electrons on WZ CdS has larger oxidation and reduction powers than the photogenerated holes and electrons on ZB CdS for photocatalytic
55 reactions, respectively, resulting in the enhancement of the rate of H_2-evolution on WZ CdS. A direct evidence for this is that the rate of H_2-evolution over this series of samples studied strictly increased with increasing content of WZ, according to the above mentioned WZ percentage composition (see Table 1). In addition,
60 the charge carrier separation capability enhanced in the mixed phase R50 sample which results in the highest photocurrent response (see Figure 8) and photocatalytic H_2-production rate. Another possible explanation is that the morphology changes from nanoparticles to multi-armed nanorods structure. The multi-
65 armed nanorods are more beneficial for the formation of mesopores and macropores than nanoparticles, which can provide efficient transport pathways to the interior void space and enhance harvesting of irradiation light by multiple scattering within the porous framework, and thus promote photocatalytic
70 hydrogen production.[48]

To provide an additional evidence for the above-mentioned photocatalytic H_2-production activity of the obtained CdS samples, the transient photocurrent responses of the R0, R15, R25 and R50 samples were investigated by several on-off cycles of
75 intermittent visible-light irradiation. Figure 8 shows a comparison of the I-t curves for the above four samples with several typical on-off cycles of intermittent irradiation. As can be seen from the I-t curves, an apparently increased boosted photocurrent response was observed for the all four samples under illumination. The
80 photocurrent value reached to a constant value as soon as the light is switched on and the photocurrent rapidly comes back to zero when the light is switched off, exhibiting a good reproducibility. This indicates that some of photogenerated electrons are transported to the back contact across the CdS

25 **Figure 7.** (a) Comparison of the photocatalytic activity of the R0, R5, R15, R25, R50, R75 and R100 samples for the photocatalytic H_2-production from aqueous lactic acid solution under visible-light irradiation. (b) Cyclic H_2-evolution curves for the R50 sample.

Figure 8. Transient photocurrent responses of the R0, R15, R25 and R50 samples in 0.5 M Na_2SO_4 aqueous solution under visible-light irradiation at 0 V vs Ag/AgCl.

Figure 9. (a) Comparison of the photocatalytic H_2-production rate of CdS-WZ, CdS-WZ/M, R50, R50/M, R50-WZ and R0 samples. TEM images of CdS-WZ (b), milled WZ CdS nanorodes CdS-WZ/M (c), and milled R50 multirods R50/M (d) samples.

samples to produce photocurrent under visible-light irradiation.[41,49] Theoretically, the hydrogen generation is directly proportional to the photocurrent. The R50 sample shows the maximum photocurrent value which agrees well with its improved H_2-production performance. This maximum photocurrent value indicates the smallest recombination and the most efficient separation of photoelectrons and holes for the R50 sample in the all four samples studied. That is, the more holes diffuse towards the R50 sample, where they are captured or trapped by reduced species in the electrolyte, the more electrons are effectively transported to the back contact.

To make a further study on the effects of crystalline phase and morphology, we clarify their roles in photocatalytic performance separately. As reported by Jang *et al.*, a CdS sample with pure WZ phase was prepared by hydrothermal method in ethylenediamine solution, labeled as CdS-WZ.[27] As shown in Figure 9b, the morphology of CdS-WZ is all of long rods. To investigate the effect of the CdS phase，R50 and CdS-WZ samples were also milled into nanoparticles (see Figure 9 c and d). Figure 9a presents a comparison of photocatalytic H_2-production rate of the aforementioned samples. Among nanoparticle samples, the photocatalytic activity are in the order CdS-WZ > R50/M > R0, indicating that the photocatalytic H_2-production activity was mainly attributed to the WZ crystalline phase on the condition of the same morphology. The R50 sample exhibit a lower H_2-production rate than that of CdS-WZ sample because of the relatively low crystallinity which determined from the corresponding XRD patterns (see Figure 10). Further observation indicates that the milled sample of R50/M significantly reduced the photocatalytic activity by 32.6%, while the H_2-evolution rate of the CdS-WZ sample increases by 21.8% after milling. It is

Table 2. Summarized specific surface area of the samples in Figure 9.

Samples	CdS-WZ	CdS-WZ/M	R50	R50/M	R50-WZ
SSA (m^2/g)	34.7	45.5	68.5	82.6	52.4
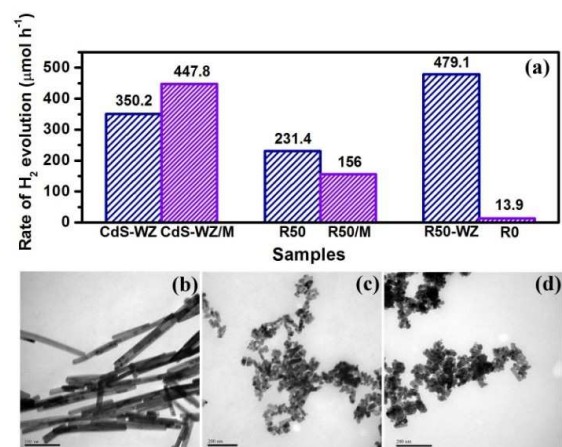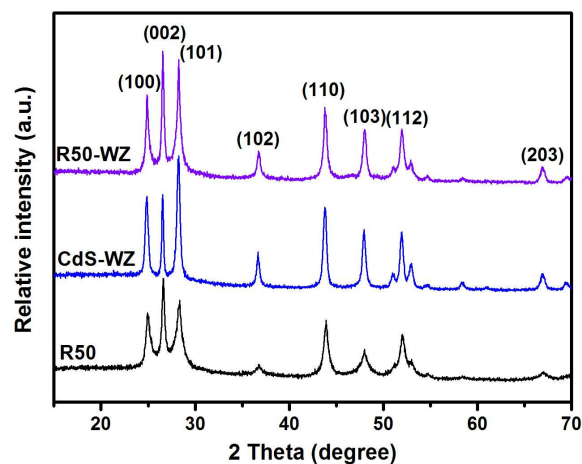
Figure 10. XRD patterns of the R50, CdS-WZ and R50-WZ.

therefore suggested that the morphology played an important role in the enhancement of H_2-production. As shown in Table 2, the trend of H_2-production activity is in disagreement with the change of surface area, indicating that the effect of specific surface area is limited. Furthermore, a multi-armed sample R50-WZ which is obtained through phase transition by calcining in a flow of N_2 at 350℃ for 2 h shows the highest H_2-production rate, which is higher than the yield of WZ particles[28] (see Figure 9). This also implies that the photocatalytic H_2-production activity is mainly attributed to the multi-armed morphology on the condition of the pure WZ phase. Therefore, it can be demonstrated from the opposite angle that the positive synergetic effects between the phase and morphology can improve the photocatalytic H_2-production activity of CdS nanomaterials.

It is noteworthy that an arm diameter of CdS multipods plays an important role in photocatalytic activity. On the one hand, small diameter of nanorods is particularly beneficial to the improvement of photocatalytic hydrogen production because the small diameter of nanorods (~6 nm) of the CdS multipods might shorten the distance between the generation center and the active

surface, which facilitate the transfer of electrons and holes to the surface active sites. On the other hand, multi-armed CdS with an arm diameter smaller than 40 nm are mainly in WZ phase, while the multipods with larger diameter are in mixed phase.[50] In our study, the diameter of rods in CdS multipods (sample R5-R50) is decreasing from ~26 nm to ~ 6 nm while little change in the length of the rods with the *R* increasing, reaching the minimum diameter of ~6 nm in sample R50. According to the above results and discussion, comparing with all the samples studied, the prepared R50 sample possesses the highest ratio of WZ phase, more multi-armed structures and the smallest diameter of rods in CdS multipods, resulting in the highest photocatalytic H_2-production activity. In fact, the photocatalytic H_2-production activity of photocatalysts should be a function of many physical parameters including the crystalline phase, crystallinity, morphology, specific surface area, pore size and distribution, etc. Consequently, in this work, the highest activity of the prepared R50 sample could be attributed to the results of the synergistic effects of WZ phase and morphology of multi-armed nanorods.

Conclusions

In summary, a series of CdS nanostructures with different content of wurtzite (WZ) and zinc blende (ZB) phase were successfully prepared by a simple solvothermal method in an ethylenediamine and ethylene glycol mixed solution. The WZ phase of CdS plays a crucial role in promoting photocatalytic hydrogen generation. The rate of H_2-evolution over this series of samples studied strictly increased with increasing content of WZ phase，achieving a maximum of 231.4 μmol h^{-1} with quantum efficiency of 28% at 420 nm for the R50 sample. The morphology of the CdS nanocrystals also had an obvious influence on the pore structure and photocatalytic H_2-production activity. Multi-armed CdS nanorods were beneficial to the formation of mesopores and macropores, thus enhancing photocatalytic H_2-production activity. This high photocatalytic H_2-production activity of the multi-armed CdS nanorods prepared at *R* = 50% could be attributed to the results of the positive synergistic effects of WZ phase and morphology of multi-armed nanorods. The multi-armed CdS nanorods prepared at *R* = 50% can be considered as a good photocatalyst for practical application because the R50 sample were stable and not photo-corroded for photocatalytic H_2-evolution from lactic acid aqueous solution after photocatalytic reaction. Considering the peculiar morphology, large specific surface area, and high photocatalytic H_2-production activity, the multi-armed CdS nanorods are also of great interest for catalysis, sensors, solar cells, nanotechnology and biomedical engineering.

Notes and references

College of Resources and Environment, Huazhong Agricultural University, Wuhan, 430070, P. R. China
E-mail: *xiangqj@mail.hzau.edu.cn*; *liufan@mail.hzau.edu.cn*

1 A. J. Bard, G. M. Whitesides, R. N. Zare and F. W. McLafferty, *Acc. Chem. Res.*, 1995, **28**, 91-91.
2 G. Hitoki, T. Takata, J. N. Kondo, M. Hara, H. Kobayashi and K. Domen, *Chem. Commun.*, 2002, 1698-1699.
3 H. G. Kim, D. W. Hwang and J. S. Lee, *J. Am. Chem. Soc.*, 2004, **126**, 8912-8913.
4 I. Tsuji, H. Kato, H. Kobayashi and A. Kudo, *J. Am. Chem. Soc.*, 2004, **126**, 13406-13413.
5 K. Maeda, T. Takata, M. Hara, N. Saito, Y. Inoue, H. Kobayashi and K. Domen, *J. Am. Chem. Soc.*, 2005, **127**, 8286-8287.
6 G. K. Mor, H. E. Prakasam, O. K. Varghese, K. Shankar and C. A. Grimes, *Nano Lett.*, 2007, **7**, 2356-2364.
7 A. Fujishima and K. Honda, *Nature*, 1972, **238**, 37-38.
8 A. Kudo and Y. Miseki, *Chem. Soc. Rev.*, 2009, **38**, 253-278.
9 Q. J. Xiang, J. G. Yu and M. Jaroniec, *Chem. Soc. Rev.*, 2012, **41**, 782-796.
10 Q. J. Xiang and J. G. Yu, *J. Phys. Chem. Lett.*, 2013, **4**, 753-759.
11 X. B. Chen, S. H. Shen, L. J. Guo and S. S. Mao, *Chem. Rev.*, 2010, **110**, 6503-6570.
12 M. Matsumura, Y. Saho and H. Tsubomura, *J. Phys. Chem.*, 1983, **87**, 3807-3808.
13 Y. P. Hong, J. Zhang, X. Wang, Y. J. Wang, Z. Lin, J. G. Yu and F. Huang, *Nanoscale*, 2012, **4**, 2859-2862.
14 N. Bao, L. Shen, T. Takata and K. Domen, *Chem. Mater.*, 2008, **20**, 110-117.
15 Q. Li, B. D. Guo, J. G. Yu, J. R. Ran, B. H. Zhang, H. J. Yan and J. R. Gong, *J. Am. Chem. Soc.*, 2011, **133**, 10878-10884.
16 T. Vossmeyer, L. Katsikas, M. Giersig, I. G. Popovic, K. Diesner, A. Chemseddine, A. Eychmüller and H. Weller, *J. Phys. Chem.*, 1994, **98**, 7665-7673.
17 X. G. Peng, L. Manna, W. D. Yang, J. Wickham, E. Scher, A. Kadavanich and A. P. Alivisatos, *Nature*, 2000, **404**, 59-61.
18 H. Q. Cao, Y. Xu, J. M. Hong, H. B. Liu, G. Yin, B. L. Li, C. Y. Tie and Z. Xu, *Adv. Mater.*, 2001, **13**, 1389-1393.
19 D. C. Pan, S. C. Jiang, L. J. An and B. Z. Jiang, *Adv. Mater.*, 2004, **16**, 982-985.
20 N. Bao, L. Shen, T. Takata, K. Domen, A. Gupta, K. Yanagisawa and C. A. Grimes, *J. Phys. Chem. C*, 2007, **111**, 17527-17534.
21 M. Muruganandham, Y. Kusumoto, C. Okamoto, A. Muruganandham, M. Abdulla-Al-Mamun and B. Ahmmad, *J. Phys. Chem. C*, 2009, **113**, 19506-19517.
22 K. Lv, J. C. Hu, X. H. Li and M. Li, *J. Mol. Catal. A*, 2012, **356**, 78-84.
23 P. Wang, J. Wang, T. S. Ming, X. F. Wang, H. G. Yu, J. G. Yu, Y. G. Wang and M. Lei, *ACS Appl. Mater. Interfaces* **2013**, 5, 2924-2929.
24 M. Ksibi, S. Rossignol, J. M. Tatibouët and C. Trapalis, *Mater. Lett.*, 2008, **62**, 4204-4206.
25 R. Banerjee, R. Jayakrishnan and P. Ayyub, *J. Phys.: Condens. Matter*, 2000, **12**, 10647.
26 E. Filatova, J. André, E. Y. Taracheva, A. Tvaladze, V. Kraizman, A. Novakovich and R. Vedrinskii, *J. Phys.: Condens. Matter*, 2004, **16**, 4597.
27 J. S. Jang, U. A. Joshi and J. S. Lee, *J. Phys. Chem. C*, 2007, **111**, 13280-13287.
28 R. J. Bandaranayake, G. W. Wen, J. Y. Lin, H. X. Jiang, and C. M. Sorensen, *Appl. Phys. Lett.*, 1995, **67**, 831-833.
29 K. Sing, D. Everett, R. Haul, L. Moscou, R. Pierotti, J. Rouquerol and T. Siemieniewska, *Pure Appl. Chem.*, 1985, **57**, 603-619.
30 J. Yang, J. H. Zeng, S. H. Yu, L. Yang, G. E. Zhou and Y. T. Qian, *Chem. Mater.*, 2000, **12**, 3259-3263.
31 A. Ghosh, S. Paul and S. Raj, *Solid State Commun.*, 2013, **154**, 25-29.
32 X. L. Wang, Z. C. Feng, D. Y. Fan, F. T. Fan and C. Li, *Cryst. Growth Des.*, 2010, **10**, 5312-5318.
33 Y. W. Jun, S. M. Lee, N. J. Kang and J. Cheon, *J. Am. Chem. Soc.*, 2001, **123**, 5150-5151.
34 Y. C. Cao and J. H. Wang, *J. Am. Chem. Soc.*, 2004, **126**, 14336-14337.
35 A. Upcher, V. Ezersky, A. Berman and Y. Golan, *Nanoscale*, 2012, **4**, 7655-7663.
36 J. W. Grebinski, K. L. Hull, J. Zhang, T. H. Kosel and M. Kuno, *Chem. Mater.*, 2004, **16**, 5260-5272.

37 P. Meakin, Fractals, Scaling and Growth Far From Equilibrium, *Cambridge University Press*, 1998.

38 O. Zelaya-Angel, J. J. Alvarado-Gil, R. Lozada-Morales, H. Vargas and A. F. Silva, *Appl. Phys. Lett.*, 1994, **64**, 291-293.

39 P. Kubelka, *J. Opt. Soc. Am.*, 1948, **38**, 448-457.

40 J. G. Yu, Q. J. Xiang and M. H. Zhou, *Appl. Catal., B*, 2009, **90**, 595-602.

41 L. Shen, N. Bao, P. E. Prevelige and A. Gupta, *J. Phys. Chem. C*, 2010, **114**, 2551-2559.

42 Q. J. Xiang, J. G. Yu and M. Jaroniec, *J. Phys. Chem. C*, 2011, **115**, 7355-7363.

43 Q. J. Xiang, B. Cheng and J. G. Yu, *Appl. Catal. B*, 2013, **138-139**, 299-303.

44 M. Ni, M. K. Leung, D. Y. Leung and K. Sumathy, *Renew. Sust. Energ. Rev.*, 2007, **11**, 401-425.

45 J. G. Yu, Y. F. Yu and B. Cheng, *RSC Adv.*, 2012, **2**, 11829-11835.

46 W. C. Lin, W. D. Yang, I. L. Huang, T. S. Wu and Z. J. Chung, *Energy Fuels*, 2009, **23**, 2192-2196.

47 Q. J. Xiang, J. G. Yu and M. Jaroniec, *J. Am. Chem. Soc.*, 2012, **134**, 6575-6578.

48 J. G. Yu, H. G. Yu, B. Cheng, X. J. Zhao, J. C. Yu and W. K. Ho, *J. Phys. Chem. B*, 2003, **107**, 13871-13879.

49 Q. J. Xiang, J. G. Yu and M. Jaroniec, *Nanoscale*, 2011, **3**, 3670-3678.

50 H. B. Chu, X. M. Li, G. D. Chen, W. W. Zhou, Y. Zhang, Z. Jin, J. J. Xu and Y. Li, *Cryst. Growth Des.*, 2005, **5**, 1801-1806.

TOC Graphics
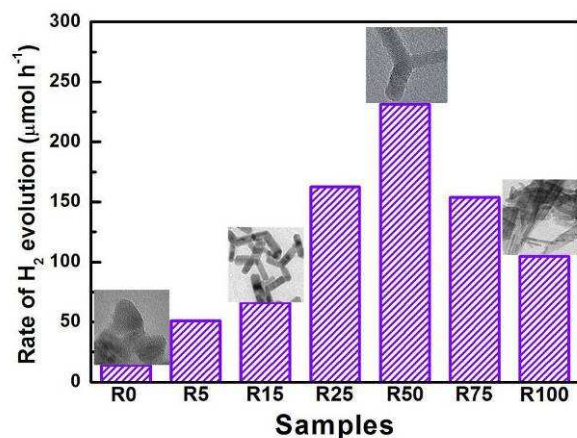
The optimized multi-armed CdS nanorods with a high percentage of wurtzite, prepared by a simple solvothermal route, exhibited high visible-light photocatalytic H_2-production performance.